Journal of Power Sources 343 (2017) 458–466

Contents lists available at ScienceDirect

Journal of Power Sources

journal homepage: www.elsevier.com/locate/jpowsour

# Co@Pt Core@Shell nanoparticles encapsulated in porous carbon derived from zeolitic imidazolate framework 67 for oxygen electroreduction in alkaline media

Likai Wang [a], Zhenghua Tang [a, b, *], Wei Yan [a], Qiannan Wang [a], Hongyu Yang [a], Shaowei Chen [a, c, **]

[a] New Energy Research Institute, School of Environment and Energy, South China University of Technology, Guangzhou Higher Education Mega Centre, Guangzhou, 510006, China
[b] Guangdong Provincial Key Laboratory of Atmospheric Environment and Pollution Control, Guangdong Provincial Engineering and Technology Research Center for Environmental Risk Prevention and Emergency Disposal, South China University of Technology, Guangzhou Higher Education Mega Centre, Guangzhou, 510006, China
[c] Department of Chemistry and Biochemistry, University of California, 1156 High Street, Santa Cruz, CA, 95064, United States

## HIGHLIGHTS

- A new type of ORR catalyst Co@Pt-NC was prepared through a facile approach.
- Characterizations confirm the structure of a Co-rich core and a Pt-rich shell.
- Co@Pt-NC demonstrated superior ORR activity and higher durability than Pt/C.
- The findings can pave a way for fabricating valuable ORR catalyst for fuel cells.

## GRAPHICAL ABSTRACT

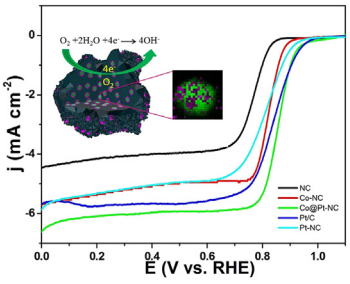


## ARTICLE INFO

*Article history:*
Received 26 September 2016
Received in revised form
14 January 2017
Accepted 18 January 2017

*Keywords:*
Co@Pt nanoparticles
Core@shell structure
Porous carbon
Oxygen electroreduction

## ABSTRACT

Nanocomposites based on Co@Pt core@shell nanoparticles encapsulated in nitrogen-doped porous carbons were prepared as a new type of high-performance electrocatalysts for oxygen reduction reaction (ORR). Controlled pyrolysis of zeolitic imidazolate framework 67 (ZIF-67) led to the formation of Co nanoparticles encapsulated in nitrogen-doped porous carbon (Co-NC), which underwent galvanic replacement reactions with $K_2PtCl_4$ forming Co@Pt core@shell nanoparticles. The surface microstructure and composition of the resulting Co@Pt-NC nanocomposite were examined by electron microscopic as well as X-ray photoelectron spectroscopic (XPS) measurements. With the Co@Pt particles encapsulated in nitrogen-doped porous carbon, the hybrids exhibited a high specific surface area and abundant catalytically active sites for ORR. Electrochemically, the specific activity and mass activity of the Co@Pt-NC composite at +0.85 V (0.145 mA $cm^{-2}$ and 71.9 A $g^{-1}$) were superior to those of commercial Pt/C

* Corresponding author. New Energy Research Institute, School of Environment and Energy, South China University of Technology, Guangzhou Higher Education Mega Centre, Guangzhou, 510006, China.
** Corresponding author. New Energy Research Institute, School of Environment and Energy, South China University of Technology, Guangzhou Higher Education Mega Centre, Guangzhou, 510006, China.
*E-mail addresses:* zhht@scut.edu.cn (Z. Tang), shaowei@ucsc.edu (S. Chen).

http://dx.doi.org/10.1016/j.jpowsour.2017.01.081
0378-7753/

Metal-organic frameworks
Pyrolysis

(0.123 mA $cm^{-2}$ and 38.4 A $g^{-1}$). Furthermore, the Co@Pt-NC composite also exhibited remarkably higher durability and more robust tolerance against methanol crossover than commercial Pt/C.



## 1. Introduction

Proton exchange membrane fuel cells have been widely considered as the next-generation energy conversion and storage systems due to their low operating temperature, high energy density, as well as negligible negative environmental impacts [1,2]. However, the oxygen reduction reaction (ORR) at the cathode is a major bottleneck that limits the fuel cell performance due to its sluggish electron-transfer kinetics and complicated reaction pathways. Therefore, it is critical to develop high-performance and robust electrocatalysts for ORR [3,4]. It has been well recognized that Pt-based nanomaterials (e. g., commercial Pt/C) are the most efficient and widely employed catalysts, but the large–scale practical applications are significantly hindered by the high costs, scarcity and low stability of Pt [5–7]. Therefore, substantial research efforts have been devoted to improving the mass activity of Pt as well as lowering the loading of Pt contents [8–14].

To improve the intrinsic activity of Pt-based catalysts and reduce the Pt loading, one effective method is to introduce secondary transition metals through the formation of Pt alloy catalysts [7,15,16]. Note that Pt alloys such as PtNi [17,18], PtCo [19,20], PtCu [21,22], PtFe [23], and PtCr [24] have been prepared and shown higher specific and mass activities than commercial Pt/C or monometallic Pt nanocatalysts. Another approach is to fabricate electrocatalysts with a core@shell structure [5,14,25]. Generally, with an atomic layer of Pt deposited on a second metal, the formation of a core@shell structure not only decreases the Pt loading, but also increases the exposure of catalytically active sites to molecular oxygen. More importantly, the core-shell interactions may be exploited for the manipulation of the electronic and surface steric/strain effects to facilitate oxygen adsorption [26,27]. In addition, using an abundant transition metal as the core can significantly lower the costs.

Notably, such core@shell nanoparticles tend to decompose, aggregate or coalesce during the electrocatalytic process due to the Ostwald ripening [28]. Such an issue can be largely mitigated by introducing carbon support, such as porous carbon [29], graphene [30], and carbon nanotubes [31], to encapsulate and/or stabilize the core-shell nanoparticles. It has been recorded that porous carbon can promote electron transfer and mass transport to facilitate the reaction kinetics [32]. Therefore, by encapsulating M@Pt (M = transition metals) core-shell nanoparticles in porous carbon support, one may be able to produce effective catalysts that not only minimize the Pt content without sacrificing the activity, but also significantly improve the long-term durability of the catalysts. This is the primary goal of the current investigation.

Herein, we describe the preparation of Co@Pt nanoparticles encapsulated in nitrogen-doped porous carbon (Co@Pt-NC) as efficient ORR catalysts. Transition metal and nitrogen-containing precursors, such as metal organic frameworks (MOFs), have been used extensively to fabricate hybrid materials for energy storage and conversion due to their uniform microporous structure and large specific surface area [33–36]. In these studies, MOFs are exploited as structural templates or matrices for the fabrication of porous carbon-based hybrid nanomaterials with the encapsulation of transition metals or metal oxides [37,38]. Note that nitrogen-doped porous carbon or honeycomb-like open porous nanostructures derived from zeolitic imidazolate frameworks (ZIF) can be easily prepared as highly efficient and durable metal-free catalysts for ORR [39–41]. Interestingly, Chen et al. demonstrated that porous carbons with a high surface area, high graphitization as well as uniform N doping could be directly obtained from pyrolysis of bimetallic MOFs [42], while Bu and Feng found that the high porosity, uniform pore walls and robust stability resulting from non-interpenetrating zirconium porphyrin frameworks can lead to enhanced ORR activity [43]. Furthermore, MOFs can impart the resultant porous structures with dual catalytic activity towards both ORR and OER (oxygen evolution reaction) in zinc-air batteries [44], or HER (hydrogen evolution reaction) and OER for water splitting [45]. Recently, Xia et al. used MOFs as precursors and successfully developed a facile, *in-situ* route to encapsulate Co@$Co_3O_4$@C core@bishell nanoparticles into a porous carbon matrix as potent electrocatalysts for ORR [46]. Inspired by these results, we prepared a new type of high-performance electrocatalysts based on Co@Pt-NC for ORR. Experimentally, controlled pyrolysis of ZIF-67 resulted in the formation of Co nanoparticles encapsulated in nitrogen-doped porous carbon. The addition of $PtCl_4^{2-}$ led to the formation of Co@Pt-NC by galvanic exchange reaction between $PtCl_4^{2-}$ and $Co^0$. The resulting Co@Pt-NC nanocomposite exhibited a high specific surface area, and hence abundant catalytically active sites for oxygen electroreduction. Furthermore, it also possessed remarkably higher durability and more robust tolerance against methanol crossover than commercial Pt/C.

## 2. Experimental section

### 2.1. Materials

Methanol and cobalt nitrate hexahydrate ($Co(NO_3)_2 \cdot 6H_2O$) were obtained from Fuchen Chemical Reagents (Tianjin, China). 2-Methylimidazole and potassium tetrachloroplatinate ($K_2PtCl_4$) were purchased from Energy Chemicals (Shanghai, China). Commercial 20 wt% Pt/C was acquired from Alfa Aesar. Distilled water with a resistivity of 18.3 MΩ·cm was used in this work. All chemicals were used as received without further purification.

### 2.2. Synthesis of ZIF-67 nanocrystals

ZIF-67 nanocrystals were synthesized according to a procedure reported previously [47]. Typically, a solution was first prepared by dissolving 1.8 g of $Co(NO_3)_2 \cdot 6H_2O$ in 12 mL of $H_2O$. Separately, a second solution was prepared where 22 g of 2-methylimidazole was dissloved in 80 mL of $H_2O$. Then, these two solutions were mixed under magnetic stirring, and the mixture was subjected to stirring for 6 h at ambient temperature, forming a purple precipitate which was collected by centrifugation and washed with deionized water and methanol multiple times. The solids were then dried at 60 °C for 24 h in a vacuum oven, affording purified ZIF-67 nanocrystals.

### 2.3. Preparation of Co-NC

The ZIF-67 nanocrystals prepared above were then subjected to

pyrolysis at controlled temperatures by following a procedure reported in the literature [37]. Typically, 1.0 g of the as-prepared ZIF-67 nanocrystals were heated at a heating rate of 1 °C $min^{-1}$ to 600 °C and sintered at this temperature for 2 h under an Ar atomsphere at a gas flow rate of 350 sccm. The product entailed Co nanoparticles encapsulated in nitrogen-doped porous carbon, which was referred to as Co-NC.

### 2.4. Preparation of Co@Pt-NC

Briefly, 50 mg of Co-NC prepared above was added to 8 mL of de-ionized water in a three-neck round-bottom flask and sonicated for 15 min to make a dispersion. The above reactor was closed and twice evacuated and purged with Ar (99.9995%, Messer) to prevent the oxidation of Co nanoparticles. Then, 10 mg of $K_2PtCl_4$ dissloved in 2 mL of de-ionized water was injected into the above solution dropwisely. The mixture was stirred at 1200 rpm for 24 h at room temperature, forming Co@Pt core@shell nanoparticles. The obtained black precipitates were then centrifuged and washed with a copious amount of water and methanol. The final product was dried under vacuum at 70 °C for 24 h, and denoted as Co@Pt-NC.

To prepare metal-free NC, 100 mg of Co-NC was added to 30 mL of a 10 wt% HCl aqueous solution which was then transferred into a 50 mL autoclave. The autoclave was sealed and heated at 170 °C for 12 h to remove Co NPs from Co-NC. The reaction solution was washed with water multiple times until the pH reached about 7. The above acid-leaching process was repeated for serveral times and the final product was denoted as NC. The Co contents in Co@Pt-NC were also removed in a similar manner, and the final product was labelled as Pt-NC.

### 2.5. Characterizations

Powder X-ray diffraction patterns (XRD) were acquired with a Bruker D8 diffractometer with Cu $K_\alpha$ radiation ($\lambda = 0.1541$ nm). X-ray photoelectron spectroscopic (XPS) measurements were conducted on a Phi X-tool instrument to characterize the surface chemical compositions and valence states. Scanning electronic microscopic (SEM) images were collected with a field–emission scanning electron microscope (FESEM, Merlin). High-resolution transmission electron microscopic (HR-TEM) measurements were conducted with a transmission electron microscope (JEOL TEM-2010). Thermogravimetric analysis (TGA) and differential scanning calorimetric (DSC) measurements were performed by using a METTLER instrument under a nitrogen flow. Barrett-Emment-Teller (BET) surface areas were estimated by using a Quantachrome Autosorb-iQ2 instrument with $N_2$ adsorption at 77 K using the Barret-Joyber-Halenda (BJH) method. Inductively coupled plasma mass spectrometric (ICP-MS) analysis was carried out with an Agilent 1260-7700e instrument.

### 2.6. Electrochemistry

All electrochemical tests were conducted on an electrochemical workstation (CHI 750E, CH Instruments Inc, Shanghai, China) with a conventional three-electrode system at ambient temperature (25 °C). A glassy carbon electrode (GCE) that was coated with the catalysts prepared above was used as the working electrode, while a Pt plate and a AgCl/Ag wire with saturated KCl (3.0 M) were employed as the counter electrode and reference electrode, respectively. To prepare the working electrode, the GCE was first polished with 0.3 and 0.05 μm alumina slurries and rinsed extensively with water. Catalyst inks were prepared as follows: 5 mg of the catalysts prepared above was dispersed in 1.0 mL ethanol containing 10 μL Nafion (5 wt %), and the above dispersion was sonicated for 30 min forming a homogeneous catalyst ink. A calculated amount (16 μL) was then dropcast onto the GCE with the loading controlled at 320 μg $cm^{-2}$ (the loading of commercial Pt/C was about 160 μg $cm^{-2}$). Cyclic voltammetric measurements were conducted in both oxygen and nitrogen saturated 0.1 M KOH aqueous solution at a scan rate of 10 mV $s^{-1}$ by the same RDE without turning within the potential range of −0.04 to +1.16 V (vs. RHE). The electrochemically active surface area (ECSA) of the catalysts were measured by the cyclic voltammetry (CV) at a scan rate of 50 mV $s^{-1}$ in an Ar-saturated 0.1 M $HClO_4$ solution at room temperature. The Ag/AgCl reference electrode was calibrated against a reversible hydrogen electrode (RHE), $E_{RHE} = E_{Ag/AgCl} + 0.196(V) + 0.0592(\mathrm{pH})$. The current densities were obtained by normalizing the voltammetric currents to the geometrical area of the GCE.

## 3. Results and discussions

A schematic of the preparation of the Co@Pt-NC nanocomposites is illustrated in Fig. 1. As displayed in Figs. S1(A and B), the as-prepared ZIF-67 [47] exhibited a well-defined polyhedral shape with the size ranging from 160 to 400 nm, and the XRD patterns (Fig. S2A) were in good accordance with those of ZIF-67 documented in the literature [47,48]. Fig. S3 depicts the nitrogen adsorption/desorption isotherm and the corresponding pore size distribution. It can be seen that ZIF-67 showed a type I isotherm (Fig. S3) and the BET surface area was estimated to be 1758.5 $m^2$ $g^{-1}$, indicating the formation of mostly micropores. After heat treatment at 600 °C, Co-NC showed a type I plus IV isotherm. The obvious uptake at low relative pressures and slight hysteresis loop at 0.9–1.0 relative pressures implies the formation of both micropores and mesopores. When $K_2PtCl_4$ was added into the aqueous dispersion of Co-NC, the micropores diminished markedly and mesopores became the dominant structure (Fig. S3). In fact, the BET surface area of Co@Pt-NC was estimated to be 254.4 $m^2$ $g^{-1}$, about half of that (423.1 $m^2$ $g^{-1}$) for Co-NC. Note that well-defined mesopores can effectively enhance the mass transport of reaction species and hence the utilization of the catalysts [49]. From TGA and DSC measurements (Fig. S4), one can see that the weight loss of ZIF-67 started to occur when the sintering temperature reached 520 °C under an $N_2$ atmosphere. Therefore, ZIF-67 nanocrystals were pyrolyzed at a somewhat higher temperature, 600 °C, for 2 h, producing Co nanoparticles encapsulated within nitrogen-doped porous carbon (Co-NC, Fig. 1). XRD measurements showed a broad diffraction peak at $2\theta = 25.9°$ (Fig. S2), which may be ascribed to the (002) crystalline planes of graphitic carbon. Additionally, there are a series of well-defined peaks at $2\theta = 44.3°$, 51.5° and 75.8°, in agreement with the diffraction patterns of metallic cobalt (JCPDS No.15-0806), indicating that Co nanoparticles were indeed formed and incorporated into the carbon skeletons. Consistent results can be observed in SEM (Fig. S1C and D) and TEM (Fig. 2A) measurements, where Co nanoparticles of 4–13 nm in diameter were encapsulated within the carbon matrix. No well-defined diffraction patterns were observed for Pt, most probably because of the formation of an ultrathin Pt shell in Co@Pt-NC [50]. It is worth noting that, the diffraction peaks of Co in Co@Pt-NC decreased slightly, as compared to those of Co@NC (dotted lines, Fig. S2B). Similar behaviors have been observed previously [51], as the Co atoms mostly resided in the core.

Galvanic replacement reaction was then exploited to grow a layer of Pt on the Co nanoparticle surface by the addition of $K_2PtCl_4$ into a Co-NC aqueous dispersion. The resulting Co@Pt-NC composites (Fig. 1) exhibited similar shapes and structures [52], as shown in Fig. 2B and Fig. S1E and F. From the inset to Fig. 2A, it can be seen that the average diameter of Co nanoparticles in Co-NC was

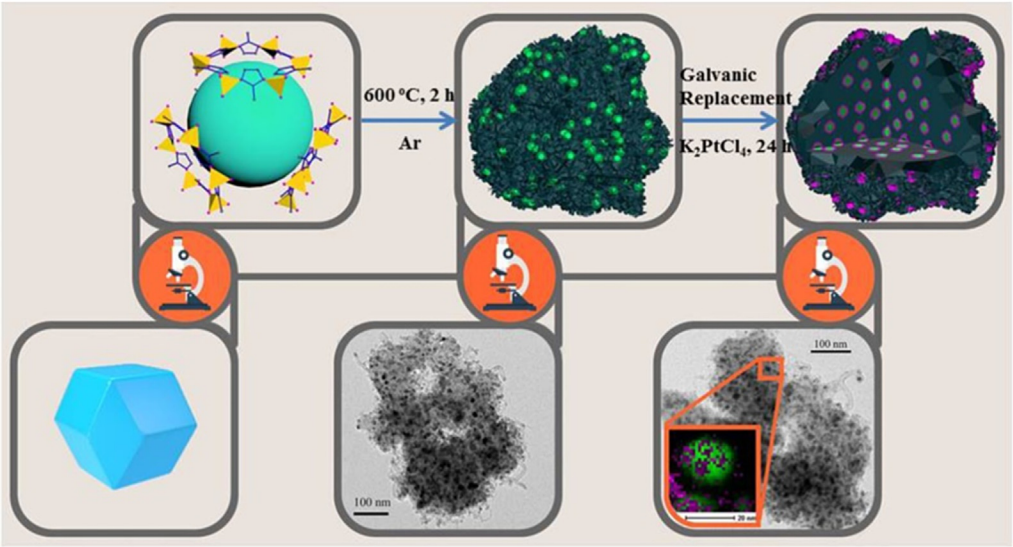


**Fig. 1.** Schematic of the preparation of Co@Pt-NC nanocomposites.

7.2 ± 2.1 nm, and remained almost unchanged (7.5 ± 2.0 nm) in Co@Pt-NC (Fig. 2B). To closely examine the elemental distribution in the Co@Pt-NC composites, elemental mapping by high-angle annular dark-field scanning transmission electron microscopic (HAADF-STEM) analysis was carried out. From the low-magnification EDX images in Fig. 2D–I, uniform distributions of nitrogen, cobalt and platinum can be observed in Co@Pt-NC, and the Co/Pt atomic ratio was estimated to be 8:1 (Fig. 2P) Note that in ICP-MS analysis a much higher Co/Pt atomic ratio was obtained at 22.10:1. The discrepancy might be due to the different sensitivity of the techniques, as EDX is mostly a surface technique with a depth of a few nanometers, while ICP-MS analysis is a better representation of the bulk property. In the present study, the Co atoms were in the core of Co@Pt nanoparticles which were encapsulated in porous carbon, rendering it difficult to detect the Co content by EDX. However, the Co atoms might be readily detected by ICP-MS measurements. High-magnification studies of a single nanoparticle (Fig. 2J–M) indeed attest the co-existence of Co and Pt, where a line scan (Fig. 2N) showed that Pt was at a markedly lower concentration, somewhat enriched at the edges whereas Co displayed a peak-shaped distribution, consistent with the formation of a Co-rich core and a Pt-rich shell.

XPS measurements were then carried out to probe the oxidation state and surface elemental composition of Co@Pt-NC (Fig. S5). From Fig. 3A, it can be seen that both Co@Pt-NC and commercial Pt/C exhibit a doublet at the binding energies of 71.8 and 74.8 eV, which can be ascribed to the $4f_{7/2}$ and $4f_{5/2}$ electrons of metallic Pt, while the pair of 72.8 and 75.8 eV and that of 75.1 and 78.2 eV are likely due to $Pt^{2+}$ and $Pt^{4+}$ in oxidized Pt ($PtO_x$), respectively [53–55]. Based on the integrated peak areas, the Pt elements in Co@Pt-NC were found to consist of 39.6% Pt(0), 37.3% PtO and 23.1% $PtO_2$, while in Pt/C, the metallic component was much higher at 60.2% Pt(0), 27.1% PtO and 12.7% $PtO_2$. The XPS spectra of C 1s electrons were depicted in Fig. S6A, where deconvolution yielded five components in Co@Pt-NC: $sp^2$ carbon (284.8 eV, 65.3%), $sp^3$ carbon (285.1 eV, 10.8%), C in C–O (286.2 eV, 11.9%), C in C=O (287.6 eV, 9.5%) and O–C=O (289.1 eV, 2.5%) [53]. In contrast, Pt/C included only $sp^2$ carbon (284.8 eV, 72.2%), $sp^3$ carbon (285.1 eV, 16.2%) and C in C–O (286.2 eV, 11.6%). These results suggest that commercial Pt/C displayed a Pt-rich surface, whereas the Co@Pt nanoparticles were likely bound to porous carbon via the ester and carbonyl moieties in the forms of COO(Pt) and C(=O)CO(Pt). Such Pt-porous carbon structures might be beneficial to the ORR catalytic activity [56].

From Fig. 3B, one can see that the Co $2p_{3/2}$ spectrum contains both metallic Co (778.8 eV) and divalent Co (781.4 eV) in the Co@Pt-NC composite, and the divalent Co might come from the surface Co atoms which interacted with the carbon matrix [57]. Note that the Co 2p electrons in Co@Pt-NC exhibited higher binding energies than those in Co-NC, suggesting charge transfer from the Co core to the Pt shell. The N 1s spectrum of Co@Pt-NC can also be deconvoluted into graphitic (400.9 eV) and pyridinic (398.9 eV) nitrogens (Fig. S6B), implying that N atoms were incorporated into the carbon skeletons. Furthermore, the concentrations of C, O, N, Co and Pt can be estimated to be 74.85%, 19.70%, 3.51%, 1.49% and 0.45% (Fig. S5), respectively, consistent with results derived from EDX measurements (Fig. 2P). The HR-TEM image in the inset to Fig. 2C displays well-defined lattice fringes with interplanar spacings of 0.21 and 0.35 nm, in agreement with the (111) crystalline planes of the metallic cobalt and the (002) crystalline planes of porous carbon, respectively. Also from Fig. 2C, one can see that the Co@Pt NPs were indeed encapsulated within multiple graphitic layers.

To examine the electrocatalytic activity of the samples, cyclic voltammetric measurements were first conducted in both oxygen and nitrogen saturated 0.1 M KOH aqueous solution at a scan rate of 10 mV $s^{-1}$. For all the samples within the potential range of −0.04 to +1.16 V (vs. RHE) in a $N_2$-saturated KOH solution, only featureless voltammetric profiles were observed (Fig. 4a and Fig. S7). In contrast, when the electrolyte was saturated with oxygen, the voltammetric profiles for all samples displayed a well-defined cathodic peak, indicating apparent electrocatalytic activity towards ORR. In particular, Co@Pt-NC displayed a cathodic peak potential of +0.87 V, much more positive than those of NC (+0.78 V), Co-NC (+0.85 V), Pt-NC (+0.86 V) as well as commercial 20% Pt/C (+0.83 V). These results indicate that Co@Pt-NC stood out as the best among the series for ORR in alkaline media.

RRDE measurements were then carried out to further evaluate the electrocatalytic activity, and the results are in good accordance with the voltammetric data. As shown in Fig. 4B, the onset potential of Co@Pt-NC (+0.99 V) was more positive than those of Pt-NC

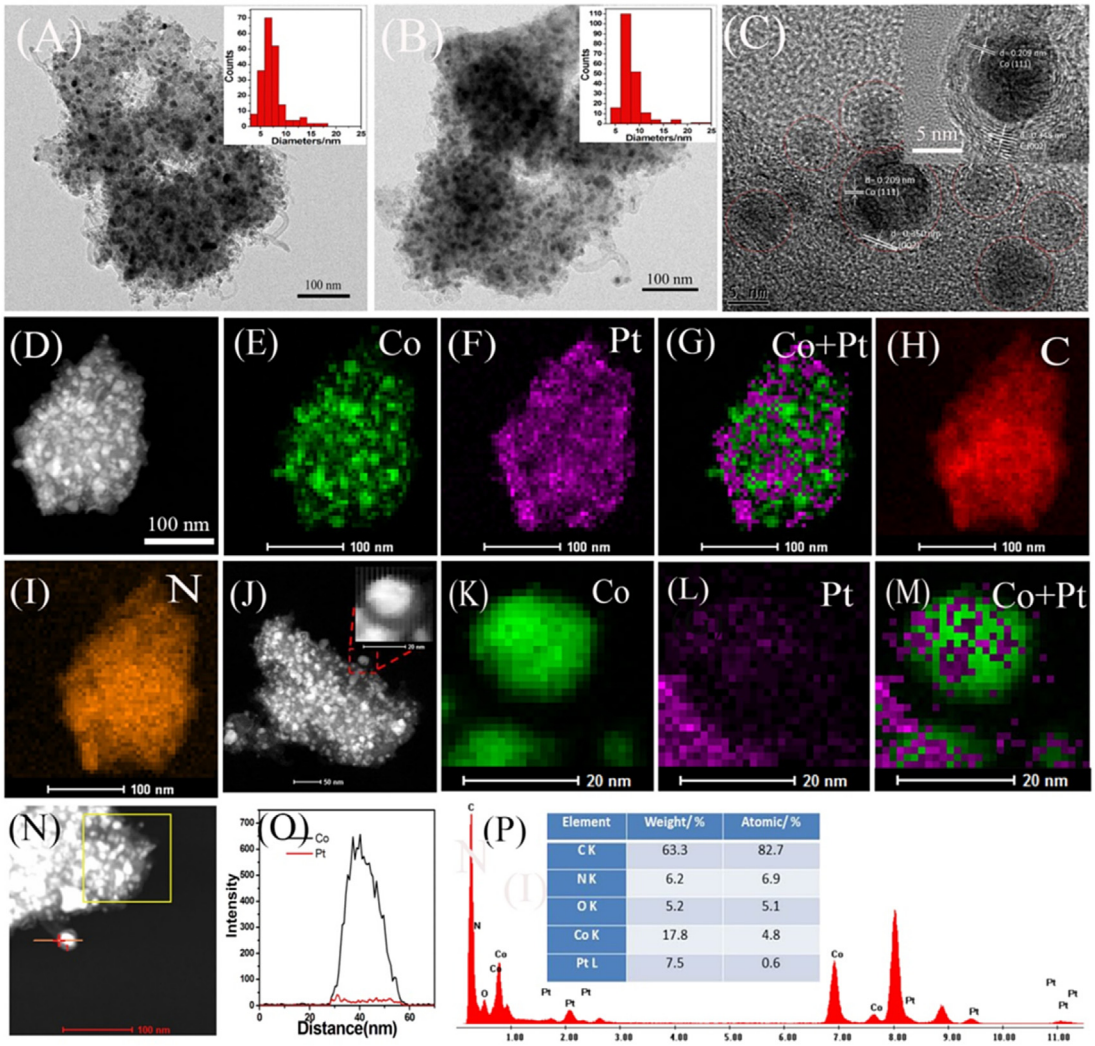


**Fig. 2.** Representative TEM images and corresponding size distributions of cobalt nanoparticles in (A) Co-NC and (B, C) Co@Pt-NC. Typical HAADF-STEM image of (D) Co@Pt-NC and (E-I) the corresponding elemental maps. Typical HAADF-STEM image of (H) Co@Pt-NC, and panels (K-M) are the corresponding elemental maps from the area with high magnification. (N) Line-scanning profiles of Pt and Co from the direction marked by a white line in (O). (P) EDX spectrum of Co@Pt-NC, and the inserted table displays the elemental content of C, O, N, Co and Pt in Co@Pt-NC.

(+0.96 V), Co-NC (+0.95 V) and NC (+0.87 V), and comparable to that of commercial 20 wt% Pt/C (+0.98 V). Furthermore, Co@Pt-NC showed a diffusion-limited current density of 5.99 mA $cm^{-2}$ and the half-wave potential ($E_{1/2}$) of +0.87 V, which were obviously superior to those of NC (4.04 mA $cm^{-2}$, +0.77 V), Co-NC (5.07 mA $cm^{-2}$, +0.82 V), Pt-NC (4.91 mA $cm^{-2}$, +0.81 V) and even commercial 20% Pt/C (5.75 mA $cm^{-2}$, +0.83 V) (Fig. 4B and Table S1). Again, Co@Pt-NC exhibited the best electrocatalytic activity for ORR among the series.

To further elucidate the ORR kinetics of the Co@Pt-NC sample, RRDE measurements were conducted with the rotation rate varied from 625 to 2025 rpm in $O_2$-saturated 0.1 M KOH. As depicted in Fig. 4C, the current density increases with increasing rotation rate [58]. The corresponding Koutecky-Levich (K-L) plots (Fig. 4C and Fig. S8) demonstrate good linearity and relatively consistent slope within the potential range of +0.40 V to +0.60 V, suggesting first-order reaction kinetics with regard to the concentration of dissolved $O_2$ in the solution. In addition, the yield of hydrogen peroxide ($H_2O_2$%) and numbers of electron transfer (n) at different potentials were calculated by the following equations:

$$n = (4I_D)/(I_D + I_R/N) \quad (1)$$

$$H_2O_2\% = (200I_R/N)/(I_R/N + I_D) \quad (2)$$

where $I_R$ is the ring current, $I_D$ is the disk current and N is the current collection efficiency (0.37) of the RRDE. The calculated results are presented in Fig. 4D. The numbers of electron transfer of Co@Pt-NC was 3.93–3.97 in the potential range of +0.40 to +0.80 V, implying that the ORR proceeded predominantly with the $4e^-$ pathway in 0.1 M KOH solution. Note that high catalyst loading may also result in an apparent four electron process due to $H_2O_2$ re-adsorption on the active sites and its further reduction [59]. Thus the possibility of a 2 + 2 pathway can't be completely ruled out. Similar behaviours were observed with commercial 20% Pt/C (n = 3.92 to 3.97). In comparison, the n values for NC, Co-NC and Pt-NC are markedly lower at 3.31 to 3.50, 3.60 to 3.85 and 3.62 to 3.86, respectively. The $H_2O_2$ yields for all samples have also been calculated by equation (2). There was only 3.1–6.5% $H_2O_2$ produced with Co@Pt-NC in the potential range of +0.40 V

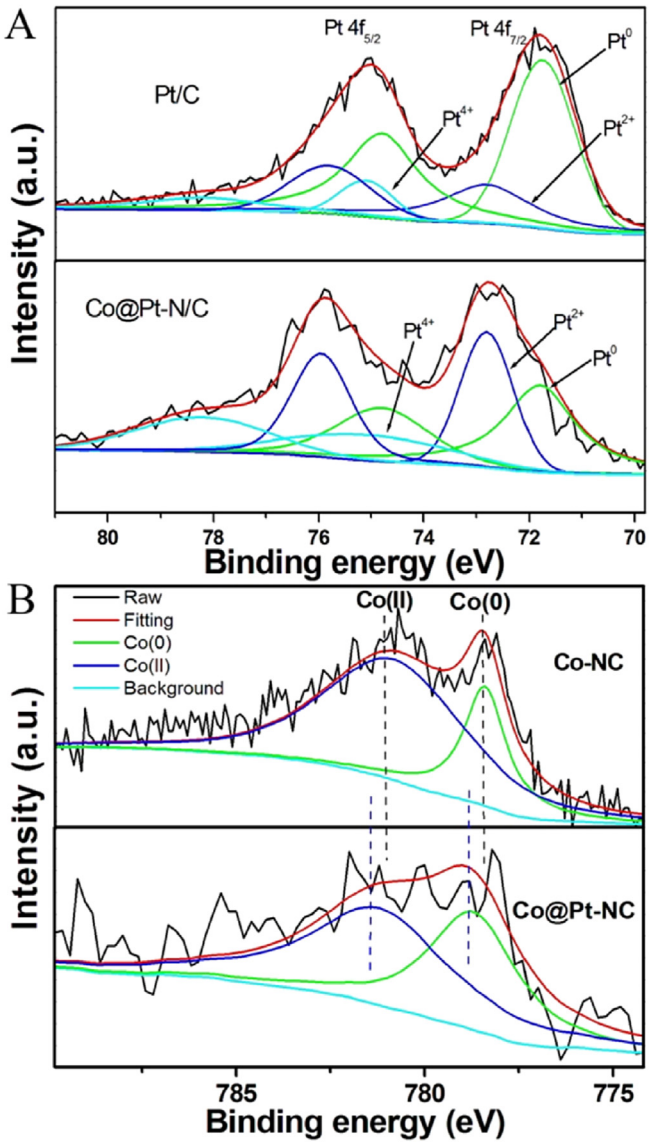


**Fig. 3.** XPS spectra for the (A) Pt 4f electrons in commercial Pt/C and Co@Pt-NC, and (B) Co 2p electrons in Co-NC and Co@Pt-NC. Black curves are experimental data and colored curves are deconvolution fits. (For interpretation of the references to colour in this figure legend, the reader is referred to the web version of this article.)

to +0.80 V, close to that of commercial Pt/C (2.5–6.1%), implying that the primary product is $OH^-$ in the ORR process. However, much higher $H_2O_2$ yields were obtained for NC (25.4–30.1%), Co-NC (6.0–19.5%) and Pt-NC (6.6–19.0%). Taken together, these results further demonstrate that Co@Pt-NC is the best electrocatalyst among the series of samples.

Furthermore, the Tafel plots were extrapolated to further evaluate the ORR kinetics. From Fig. 4e, it can be seen that the Tafel plots showed two linear segments in the low and high overpotential regimes [3,5]. In the low overpotential range, the slopes were found at 71.4 mV $dec^{-1}$ for Co@Pt-NC and 73.8 mV $dec^{-1}$ for Pt/C, suggesting that the reaction kinetics in the electrocatalytic reduction of oxygen was determined largely by a pseudo two-electron reaction. However, at potentials below +0.85 V, the Tafel slopes was found at 117.5 mV $dec^{-1}$ for Co@Pt-NC and 109.3 mV $dec^{-1}$ for Pt/C, implying that the reaction rate-determining step is the first electron transfer to oxygen molecules [14,60].

Furthermore, the kinetic current can be readily quantified from the ORR polarization curves by using the Koutecky-Levich (K-L) equation [61], from which the specific and mass activity may be calculated by normalizing the kinetic current to the electrochemically active surface area (ECSA, which was 31.2 and 49.6 $m^2\ g^{-1}$ for Pt/C and Co@Pt-NC, respectively, Fig. S9) [62] and the Pt loading. Fig. 4f compares the specific and mass activity between Co@Pt-NC (0.145 mA $cm^{-2}$ and 71.9 A $g^{-1}$) and commercial Pt/C (0.123 mA $cm^{-2}$ and 38.4 A $g^{-1}$) at +0.85 V. It is clear that Co@Pt-NC exhibited a better ORR performance than commercial Pt/C [63].

In addition, the ORR activity was also tested and compared in an oxygen-saturated 0.5 M $H_2SO_4$ solution. Among the series of samples, Co@Pt-NC displayed the best performance with an onset potential of +0.94 V and a half-wave potential of +0.78 V, which was also comparable to that of commercial Pt/C in acid media (Fig. S10A). The numbers of electron transfer of Co@Pt-NC was 3.95–4.00 at +0.40 V to +0.60 V (Fig. S10B), similar to those of commercial 20 wt% Pt/C (3.94–3.99). It suggests that ORR also proceeded through the $4e^-$ pathway in 0.5 M $H_2SO_4$. Fig. S10C presents the LSV curves of Co@Pt-NC with the rotation rate varied from 625 to 2025 rpm in the $O_2$-saturated 0.5 M $H_2SO_4$ solution. Note that the corresponding K-L plots (Fig. S10D) also demonstrate good linearity, and relatively consistent slope was obtained within the potential range of +0.30 to +0.50 V. Moreover, after 40,000 s of continuous operation (Fig. S11), the Co@Pt-NC composite displayed better long-term durability than commercial Pt/C (average size 3.0 ± 0.8 nm, Fig. S12).

The remarkably high ORR activity of Co@Pt-NC may be accounted for by the following factors: First, the outer layer of Pt contributed to various catalytically active sites [64–66]; Second, the synergistic interactions between the Co core and the Pt shell tuned the electronic effects on the Pt shell [65], which facilitated the 4-electron transfer kinetics, as evidenced by the shift of the Pt 4f electron binding energy observed in XPS measurements; and finally, the nitrogen-doped porous carbon not only served as a support or stabilizer, but also played a critical role in metal-nitrogen-carbon interactions [67–69]. It has been postulated that such metal-nitrogen-carbon interactions can significantly lower the oxygen dissociation energy by accelerating the charge transfer from Pt atoms to oxygen molecules [3].

The Co@Pt-NC composite also displayed excellent long-term durability, as manifested in chronoamperometric measurements at +0.6 V in an $O_2$-saturated 0.1 M KOH aqueous solution. From Fig. 5A, it can be seen that the Pt/C electrode showed a rapid decrease of the current density by about 29% after 40,000 s of continuous operation. However, there was only about 12% loss for the Co@Pt-NC under the same conditions, indicating more robust stability of Co@Pt-NC for ORR. Co@Pt-NC also showed stronger resistance against methanol crossover. The chronoamperometric curve of commercial Pt/C showed a sharp decrease upon the addition of 1 M methanol at the rotation rate of 900 rpm at +0.60 V in an oxygen-saturated 0.1 M KOH solution (Fig. 5B). In contrast, the current density of the Co@Pt-NC electrode remained almost invariant, indicating that Co@Pt-NC possessed remarkably higher tolerance against methanol poisoning. Finally, to assess the durability of the catalyst, accelerated durability tests were carried out by cycling the catalyst over the potential range of +0.6 to +1.0 V at 50 mV $s^{-1}$ in an oxygen-saturated 0.1 M KOH solution. As shown in Fig. 5C, the half-wave potential of commercial Pt/C shifted negatively by 26 mV after 5000 continuous cycles, while that of Co@Pt-NC displayed a much smaller negative shift of only 17 mV (Fig. 5D). The minimal methanol poisoning might be ascribed to the unique structure of Co@Pt-NC where Pt layers were likely sandwiched between the Co core and the carbon overlayer, with additional contributions from the synergistic interactions between the Co@Pt core-shell [70].

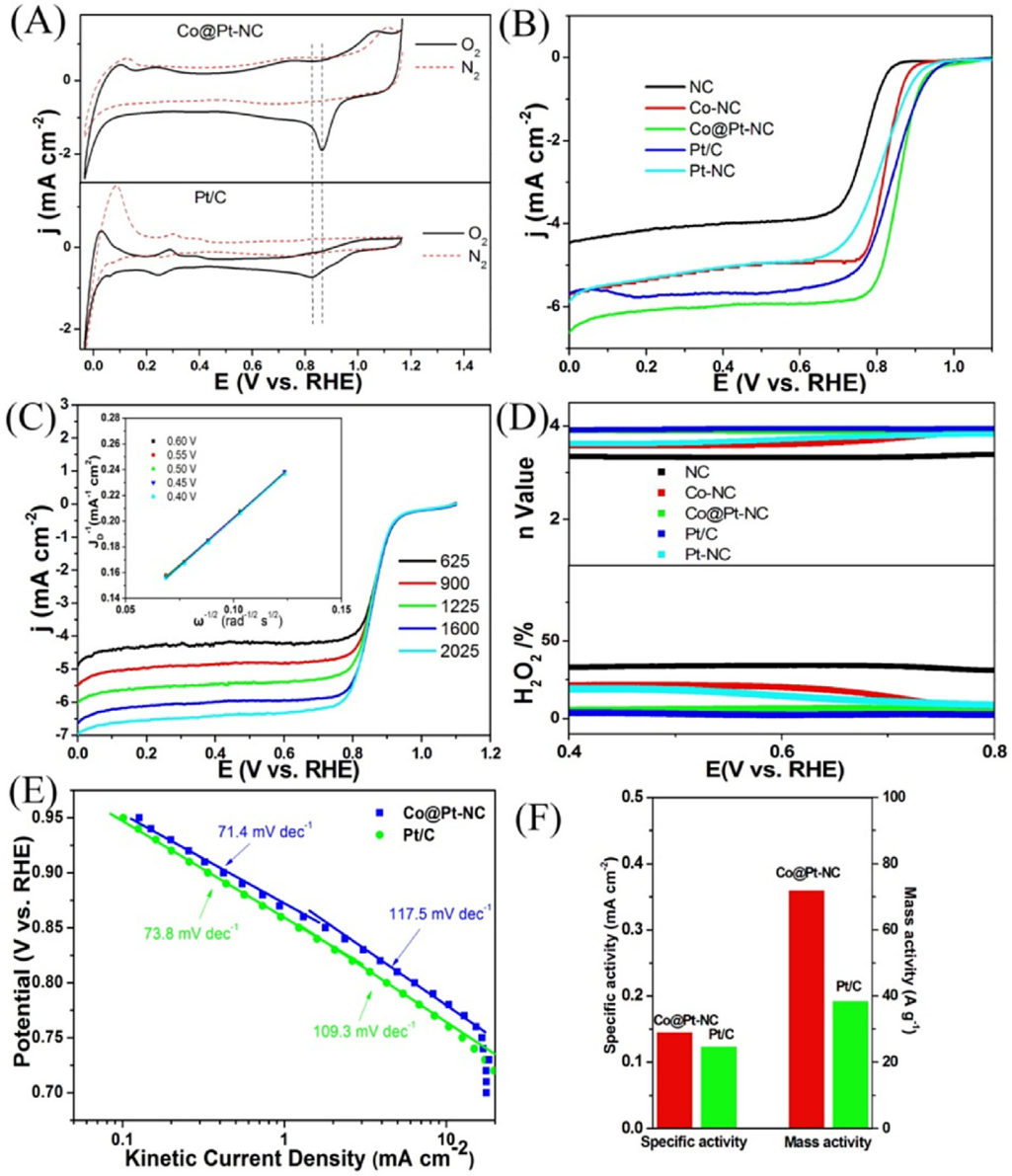


**Fig. 4.** (A) CV curves of Co@Pt-NC and commercial Pt/C in a $O_2$ or $N_2$ saturated 0.1 M KOH solution at a scan rate of 10 mV $s^{-1}$ (B) LSV curves of NC, Co-NC, Pt-NC, Co@Pt-NC and commercial Pt/C in a $O_2$-saturated 0.1 M KOH solution at a rotation rate of 1600 rpm. (C) LSV curves of Co@Pt-NC at different rotation rates from 625 to 2025 rpm (inset displays the K-L plots between +0.40 V and +0.60 V). (D) Numbers of electron transfer and the corresponding $H_2O_2$ yields at different potentials, (E) Tafel plots and (F) comparison of specific activity and mass activity of Co@Pt-NC and commercial Pt/C.

## 4. Conclusions

In summary, we have prepared a high-performance ORR catalyst based on Co@Pt core@shell nanoparticles encapsulated in nitrogen-doped porous carbons. Controlled pyrolysis of ZIF-67 resulted in the formation of Co nanoparticles encapsulated in porous carbon, which upon galvanic replacement reaction with $K_2PtCl_4$ formed Co@Pt-NC nanocomposites. The surface microstructure and composition of Co@Pt-NC were then examined by TEM, SEM, EDX as well as XPS measurements, confirming the formation of a Co core and a Pt shell in the resulting nanoparticles that were encapsulated within layers of porous carbon. Significantly, electrochemical tests showed that the specific activity and mass activity of the Co@Pt-NC composite at +0.85 V (0.145 mA $cm^{-2}$ and 71.9 A $g^{-1}$) were superior to those of commercial Pt/C (0.123 mA $cm^{-2}$ and 38.4 A $g^{-1}$). Furthermore, the Co@Pt-NC composite also possessed remarkably higher durability and more robust tolerance to methanol crossover than Pt/C. Taken together, these results suggest an effective way to the rational design and fabrication of high-performance, cost-effective and robust cathode catalyst for fuel cell applications.

## Acknowledgements

Z. H. T. thanks financial support from the National Natural Science Foundation of China (21501059), Guangdong Natural Science Funds for Distinguished Young Scholars (No. 2015A030306006), Guangdong Innovative and Entrepreneurial Research Team Program (No. 2014ZT05N200), as well as the Fundamental Research Funds for Central Universities (SCUT Grant No. 2015PT026). S. W. C. acknowledges the National Natural Science Foundation of China for partial support of the work (21528301).

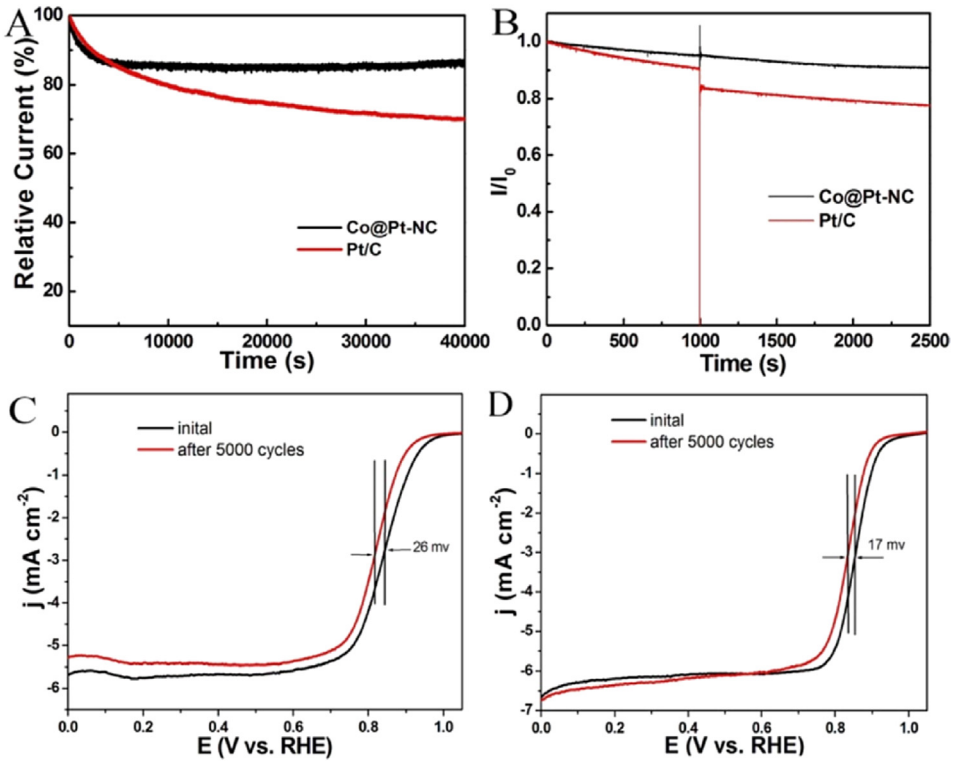


**Fig. 5.** (A) Current-time (*i-t*) curve and (B) Chronoamperometric response to addition of 1 M methanol of Co@Pt-NC and commercial Pt/C with a rotation speed of 900 rpm at +0.60 V in an oxygen-saturated 0.1 M KOH solution. The accelerated durability tests (ADT) of commercial Pt/C (C) and Co@Pt-NC (D) were carried out by before and after 5000 cycles between 0.6 and 1.0 V at a scan rate of 50 mV $s^{-1}$ with a rotation speed of 1600 rpm in an oxygen-saturated 0.1 M KOH solution.

## Appendix A. Supplementary data

Supplementary data related to this article can be found at http://dx.doi.org/10.1016/j.jpowsour.2017.01.081.

## References

[1] M. Winter, R.J. Brodd, What are batteries, fuel cells, and supercapacitors? Chem. Rev. 104 (2004) 4245–4270.
[2] A. Kraytsberg, Y. Ein-Eli, Review of advanced materials for proton exchange membrane fuel cells, Energy Fuels 28 (2014) 7303–7330.
[3] M. Liu, R. Zhang, W. Chen, Graphene-supported nanoelectrocatalysts for fuel cells: synthesis, properties, and applications, Chem. Rev. 114 (2014) 5117–5160.
[4] Y. Jiao, Y. Zheng, M. Jaroniec, S.Z. Qiao, Design of electrocatalysts for oxygen- and hydrogen-involving energy conversion reactions, Chem. Soc. Rev. 44 (2015) 2060–2086.
[5] S. Guo, S. Zhang, S. Sun, Tuning nanoparticle catalysis for the oxygen reduction reaction, Angew Chem, Int. Ed. 52 (2013) 8526–8544.
[6] C.-H. Cui, S.-H. Yu, Engineering interface and surface of noble metal nanoparticle nanotubes toward enhanced catalytic activity for fuel cell applications, Acc. Chem. Res. 46 (2013) 1427–1437.
[7] C. Wang, N.M. Markovic, V.R. Stamenkovic, Advanced platinum alloy electrocatalysts for the oxygen reduction reaction, ACS Catal. 2 (2012) 891–898.
[8] V.R. Stamenkovic, B. Fowler, B.S. Mun, G. Wang, P.N. Ross, C.A. Lucas, N.M. Marković, Improved oxygen reduction activity on $Pt_3Ni(111)$ via increased surface site availability, Science 315 (2007) 493–497.
[9] V.R. Stamenkovic, B.S. Mun, M. Arenz, K.J.J. Mayrhofer, C.A. Lucas, G. Wang, P.N. Ross, N.M. Markovic, Trends in electrocatalysis on extended and nanoscale Pt-bimetallic alloy surfaces, Nat. Mater 6 (2007) 241–247.
[10] B. Lim, M. Jiang, P.H.C. Camargo, E.C. Cho, J. Tao, X. Lu, Y. Zhu, Y. Xia, Pd-Pt bimetallic nanodendrites with high activity for oxygen reduction, Science 324 (2009) 1302–1305.
[11] L. Bu, S. Guo, X. Zhang, X. Shen, D. Su, G. Lu, X. Zhu, J. Yao, J. Guo, X. Huang, Surface engineering of hierarchical platinum-cobalt nanowires for efficient electrocatalysis, Nat. Commun. 7 (2016) 11850.
[12] X. Huang, Z. Zhao, L. Cao, Y. Chen, E. Zhu, Z. Lin, M. Li, A. Yan, A. Zettl, Y.M. Wang, X. Duan, T. Mueller, Y. Huang, High-performance transition metal–doped $Pt_3Ni$ octahedra for oxygen reduction reaction, Science 348 (2015) 1230–1234.
[13] G. He, Y. Song, K. Liu, A. Walter, S. Chen, S. Chen, Oxygen reduction catalyzed by platinum nanoparticles supported on graphene quantum dots, ACS Catal. 3 (2013) 831–838.
[14] M. Shao, Q. Chang, J.-P. Dodelet, R. Chenitz, Recent advances in electrocatalysts for oxygen reduction reaction, Chem. Rev. 116 (2016) 3594–3657.
[15] T. Kaito, H. Tanaka, H. Mitsumoto, S. Sugawara, K. Shinohara, H. Ariga, H. Uehara, S. Takakusagi, K. Asakura, Situ X-ray absorption fine structure analysis of PtCo, PtCu, and PtNi alloy electrocatalysts: the correlation of enhanced oxygen reduction reaction activity and structure, J. Phys. Chem. C 120 (2016) 11519–11527.
[16] V. Čolić, A.S. Bandarenka, Pt alloy electrocatalysts for the oxygen reduction reaction: from model surfaces to nanostructured systems, ACS Catal. 6 (2016) 5378–5385.
[17] C. Cui, L. Gan, H.-H. Li, S.-H. Yu, M. Heggen, P. Strasser, Octahedral PtNi nanoparticle catalysts: exceptional oxygen reduction activity by tuning the alloy particle surface composition, Nano Lett. 12 (2012) 5885–5889.
[18] K. Eid, H. Wang, V. Malgras, Z.A. Alothman, Y. Yamauchi, L. Wang, Facile synthesis of porous dendritic bimetallic platinum–nickel nanocrystals as efficient catalysts for the oxygen reduction reaction, Chem. Asian J. 11 (2016) 1388–1393.
[19] S.-I. Choi, R. Choi, S.W. Han, J.T. Park, Synthesis and characterization of $Pt_9Co$ nanocubes with high activity for oxygen reduction, Chem. Commun. 46 (2010) 4950–4952.
[20] F.H.B. Lima, J.F.R. de Castro, L.G.R.A. Santos, E.A. Ticianelli, Electrocatalysis of oxygen reduction on carbon-supported Pt–Co nanoparticles with low Pt content, J. Power Sources 190 (2009) 293–300.
[21] P. Strasser, S. Koh, T. Anniyev, J. Greeley, K. More, C. Yu, Z. Liu, S. Kaya, D. Nordlund, H. Ogasawara, M.F. Toney, A. Nilsson, Lattice-strain control of the activity in dealloyed core–shell fuel cell catalysts, Nat. Chem. 2 (2010) 454–460.
[22] M. Oezaslan, P. Strasser, Activity of dealloyed $PtCo_3$ and $PtCu_3$ nanoparticle electrocatalyst for oxygen reduction reaction in polymer electrolyte membrane fuel cell, J. Power Sources 196 (2011) 5240–5249.
[23] D.Y. Chung, S.W. Jun, G. Yoon, S.G. Kwon, D.Y. Shin, P. Seo, J.M. Yoo, H. Shin, Y.-H. Chung, H. Kim, B.S. Mun, K.-S. Lee, N.-S. Lee, S.J. Yoo, D.-H. Lim, K. Kang, Y.-E. Sung, T. Hyeon, Highly durable and active PtFe nanocatalyst for electrochemical oxygen reduction reaction, J. Am. Chem. Soc. 137 (2015) 15478–15485.
[24] R.C. Koffi, C. Coutanceau, E. Garnier, J.M. Léger, C. Lamy, Synthesis, characterization and electrocatalytic behaviour of non-alloyed PtCr methanol tolerant nanoelectrocatalysts for the oxygen reduction reaction (ORR), Electrochim. Acta 50 (2005) 4117–4127.

[25] J. Wu, H. Yang, Platinum-based oxygen reduction electrocatalysts, Acc. Chem. Res. 46 (2013) 1848–1857.
[26] N. Kristian, Y. Yu, J.-M. Lee, X. Liu, X. Wang, Synthesis and characterization of $Co_{core}$–$Pt_{shell}$ electrocatalyst prepared by spontaneous replacement reaction for oxygen reduction reaction, Electrochim. Acta 56 (2010) 1000–1007.
[27] X. Zhang, H. Wang, J. Key, V. Linkov, S. Ji, X. Wang, Z. Lei, R. Wang, Strain effect of core-shell Co@Pt/C nanoparticle catalyst with enhanced electrocatalytic activity for methanol oxidation, J. Electrochem. Soc. 159 (2012) B270–B276.
[28] C. Koenigsmann, S.S. Wong, One-dimensional noble metal electrocatalysts: a promising structural paradigm for direct methanol fuel cells, Energy Environ. Sci. 4 (2011) 1161–1176.
[29] Z. Li, C. He, M. Cai, S. Kang, P.K. Shen, A strategy for easy synthesis of carbon supported Co@Pt core–shell configuration as highly active catalyst for oxygen reduction reaction, Int. J. Hydrogen Energy 37 (2012) 14152–14160.
[30] J. Jin, X. Fu, Q. Liu, J. Zhang, A highly active and stable electrocatalyst for the oxygen reduction reaction based on a graphene-supported G-$C_3N_4$@cobalt oxide core-shell hybrid in alkaline solution, J. Mater. Chem. A 1 (2013) 10538–10545.
[31] J. Xiao, L. Wan, X. Wang, Q. Kuang, S. Dong, F. Xiao, S. Wang, Mesoporous $Mn_3O_4$-CoO core-shell spheres wrapped by carbon nanotubes: a high performance catalyst for the oxygen reduction reaction and CO oxidation, J. Mater. Chem. A 2 (2014) 3794–3800.
[32] H. Yin, H. Tang, D. Wang, Y. Gao, Z. Tang, Facile synthesis of surfactant-free Au cluster/graphene hybrids for high-performance oxygen reduction reaction, ACS Nano 6 (2012) 8288–8297.
[33] W. Xia, A. Mahmood, R. Zou, Q. Xu, Metal-organic frameworks and their derived nanostructures for electrochemical energy storage and conversion, Energy Environ. Sci. 8 (2015) 1837–1866.
[34] S.-L. Li, Q. Xu, Metal-organic frameworks as platforms for clean energy, Energy Environ. Sci. 6 (2013) 1656–1683.
[35] C. Combelles, M.B. Yahia, L. Pedesseau, M.L. Doublet, Design of electrode materials for lithium-ion batteries: the example of Metal–Organic frameworks, J. Phys. Chem. C 114 (2010) 9518–9527.
[36] Y. Ren, G.H. Chia, Z. Gao, Metal–organic frameworks in fuel cell technologies, Nano Today 8 (2013) 577–597.
[37] K. Shen, L. Chen, J. Long, W. Zhong, Y. Li, MOFs-templated Co@Pd core–shell NPs embedded in N-Doped carbon matrix with superior hydrogenation activities, ACS Catal. 5 (2015) 5264–5271.
[38] S. Ma, G.A. Goenaga, A.V. Call, D.-J. Liu, Cobalt imidazolate framework as precursor for oxygen reduction reaction electrocatalysts, Chem. Eur. J. 17 (2011) 2063–2067.
[39] P. Zhang, F. Sun, Z. Xiang, Z. Shen, J. Yun, D. Cao, ZIF-derived in situ nitrogen-doped porous carbons as efficient metal-free electrocatalysts for oxygen reduction reaction, Energy Environ. Sci. 7 (2014) 442–450.
[40] H.-x. Zhong, J. Wang, Y.-w. Zhang, W.-l. Xu, W. Xing, D. Xu, Y.-f. Zhang, X.-b. Zhang, ZIF-8 derived graphene-based nitrogen-doped porous carbon sheets as highly efficient and durable oxygen reduction electrocatalysts, Angew. Chem. Int. Ed. 53 (2014) 14235–14239.
[41] Q.-L. Zhu, W. Xia, T. Akita, R. Zou, Q. Xu, Metal-organic framework-derived honeycomb-like open porous nanostructures as precious-metal-free catalysts for highly efficient oxygen electroreduction, Adv. Mater 28 (2016) 6391–6398.
[42] Y.-Z. Chen, C. Wang, Z.-Y. Wu, Y. Xiong, Q. Xu, S.-H. Yu, H.-L. Jiang, From bimetallic metal-organic framework to porous carbon: high surface area and multicomponent active dopants for excellent electrocatalysis, Adv. Mater 27 (2015) 5010–5016.
[43] Q. Lin, X. Bu, A. Kong, C. Mao, X. Zhao, F. Bu, P. Feng, New heterometallic zirconium metalloporphyrin frameworks, their heteroatom-activated, high-surface-area carbon derivatives, J. Am. Chem. Soc. 137 (2015) 2235–2238.
[44] F. Meng, H. Zhong, D. Bao, J. Yan, X. Zhang, In situ coupling of strung $Co_4N$ and intertwined N–C fibers toward free-standing bifunctional cathode for robust, efficient, and flexible Zn–Air batteries, J. Am. Chem. Soc. 138 (2016) 10226–10231.
[45] L. Jiao, Y.-X. Zhou, H.-L. Jiang, Metal-organic framework-based CoP/reduced graphene oxide: high-performance bifunctional electrocatalyst for overall water splitting, Chem. Sci. 7 (2016) 1690–1695.
[46] W. Xia, R. Zou, L. An, D. Xia, S. Guo, A metal-organic framework route to in situ encapsulation of Co@$Co_3O_4$@C Core@bishell nanoparticles into a highly ordered porous carbon matrix for oxygen reduction, Energy Environ. Sci. 8 (2015) 568–576.
[47] J. Qian, F. Sun, L. Qin, Hydrothermal synthesis of zeolitic imidazolate framework-67 (ZIF-67), Nanocrystals. Mater. Lett. 82 (2012) 220–223.
[48] R. Banerjee, A. Phan, B. Wang, C. Knobler, H. Furukawa, M. O'Keeffe, O.M. Yaghi, High-throughput synthesis of zeolitic imidazolate frameworks and application to $CO_2$ capture, Science 319 (2008) 939–943.
[49] K. Shen, W. Qian, N. Wang, C. Su, F. Wei, Fabrication of c-axis oriented ZSM-5 hollow fibers based on an in situ solid–solid transformation mechanism, J. Am. Chem. Soc. 135 (2013) 15322–15325.
[50] X. Tian, J. Luo, H. Nan, H. Zou, R. Chen, T. Shu, X. Li, Y. Li, H. Song, S. Liao, R.R. Adzic, Transition metal nitride coated with atomic layers of Pt as a low-cost, highly stable electrocatalyst for the oxygen reduction reaction, J. Am. Chem. Soc. 138 (2016) 1575–1583.
[51] Y. Chen, F. Yang, Y. Dai, W. Wang, S. Chen, Ni@Pt core–shell nanoparticles: synthesis, structural and electrochemical properties, J. Phys. Chem. C 112 (2008) 1645–1649.
[52] D. Wang, H.L. Xin, Y. Yu, H. Wang, E. Rus, D.A. Muller, H.D. Abruña, Pt-decorated PdCo@Pd/C core–shell nanoparticles with enhanced stability and electrocatalytic activity for the oxygen reduction reaction, J. Am. Chem. Soc. 132 (2010) 17664–17666.
[53] B. Singh, L. Murad, F. Laffir, C. Dickinson, E. Dempsey, Pt based nanocomposites (Mono/bi/tri-metallic) decorated using different carbon supports for methanol electro-oxidation in acidic and basic media, Nanoscale 3 (2011) 3334–3349.
[54] I.A. Khan, Y. Qian, A. Badshah, M.A. Nadeem, D. Zhao, Highly porous carbon derived from MOF-5 as a support of ORR electrocatalysts for fuel cells, ACS Appl. Mater. Interfaces 8 (2016) 17268–17275.
[55] Y. Xin, J.-g. Liu, Y. Zhou, W. Liu, J. Gao, Y. Xie, Y. Yin, Z. Zou, Preparation and characterization of Pt supported on graphene with enhanced electrocatalytic activity in fuel cell, J. Power Sources 196 (2011) 1012–1018.
[56] R.V. Hull, L. Li, Y. Xing, C.C. Chusuei, Pt nanoparticle binding on functionalized multiwalled carbon nanotubes, Chem. Mater 18 (2006) 1780–1788.
[57] X. Wang, J. Zhou, H. Fu, W. Li, X. Fan, G. Xin, J. Zheng, X. Li, MOF derived catalysts for electrochemical oxygen reduction, J. Mater. Chem. A 2 (2014) 14064–14070.
[58] J. Liu, X. Sun, P. Song, Y. Zhang, W. Xing, W. Xu, High-performance oxygen reduction electrocatalysts based on cheap carbon black, nitrogen, and trace iron, Adv. Mater 25 (2013) 6879–6883.
[59] T. Poux, A. Bonnefont, G. Kéranguéven, G.A. Tsirlina, E.R. Savinova, Electrocatalytic oxygen reduction reaction on perovskite oxides: series versus direct pathway, ChemPhysChem 15 (2014) 2108–2120.
[60] M. Zhou, H.-L. Wang, S. Guo, Towards high-efficiency nanoelectrocatalysts for oxygen reduction through engineering advanced carbon nanomaterials, Chem. Soc. Rev. 45 (2016) 1273–1307.
[61] R. Li, Z. Wei, X. Gou, Nitrogen and phosphorus dual-doped graphene/carbon nanosheets as bifunctional electrocatalysts for oxygen reduction and evolution, ACS Catal. 5 (2015) 4133–4142.
[62] K.A. Kuttiyiel, K. Sasaki, Y. Choi, D. Su, P. Liu, R.R. Adzic, Nitride stabilized PtNi core–shell nanocatalyst for high oxygen reduction activity, Nano Lett. 12 (2012) 6266–6271.
[63] J. Hu, L. Wu, K.A. Kuttiyiel, K.R. Goodman, C. Zhang, Y. Zhu, M.B. Vukmirovic, M.G. White, K. Sasaki, R.R. Adzic, Increasing stability and activity of core–shell catalysts by preferential segregation of oxide on edges and vertexes: oxygen reduction on Ti–Au@Pt/C, J. Am. Chem. Soc. 138 (2016) 9294–9300.
[64] S.M. Alia, S. Pylypenko, K.C. Neyerlin, D.A. Cullen, S.S. Kocha, B.S. Pivovar, Platinum-coated cobalt nanowires as oxygen reduction reaction electrocatalysts, ACS Catal. 4 (2014) 2680–2686.
[65] D. Wang, H.L. Xin, R. Hovden, H. Wang, Y. Yu, D.A. Muller, F.J. DiSalvo, H.D. Abruña, Structurally ordered intermetallic platinum–cobalt core–shell nanoparticles with enhanced activity and stability as oxygen reduction electrocatalysts, Nat. Mater 12 (2013) 81–87.
[66] K. Sasaki, H. Naohara, Y. Choi, Y. Cai, W.-F. Chen, P. Liu, R.R. Adzic, Highly stable Pt monolayer on PdAu nanoparticle electrocatalysts for the oxygen reduction reaction, Nat. Commun. 3 (2012) 1115.
[67] H.-W. Liang, W. Wei, Z.-S. Wu, X. Feng, K. Müllen, Mesoporous metal–nitrogen-doped carbon electrocatalysts for highly efficient oxygen reduction reaction, J. Am. Chem. Soc. 135 (2013) 16002–16005.
[68] W. Niu, L. Li, X. Liu, N. Wang, J. Liu, W. Zhou, Z. Tang, S. Chen, Mesoporous N-doped carbons prepared with thermally removable nanoparticle templates: an efficient electrocatalyst for oxygen reduction reaction, J. Am. Chem. Soc. 137 (2015) 5555–5562.
[69] W.-J. Jiang, L. Gu, L. Li, Y. Zhang, X. Zhang, L.-J. Zhang, J.-Q. Wang, J.-S. Hu, Z. Wei, L.-J. Wan, Understanding the high activity of Fe–N–C electrocatalysts in oxygen reduction: Fe/$Fe_3C$ nanoparticles boost the activity of Fe–$N_x$, J. Am. Chem. Soc. 138 (2016) 3570–3578.
[70] J.R.C. Salgado, E. Antolini, E.R. Gonzalez, Carbon supported Pt–Co alloys as methanol-resistant oxygen-reduction electrocatalysts for direct methanol fuel cells, Appl. Catal. B Environ. 57 (2005) 283–290.